UC Davis
UC Davis Previously Published Works

Title
Super-Resolution Photothermal Patterning in Conductive Polymers Enabled by Thermally Activated Solubility

Permalink
https://escholarship.org/uc/item/1h31655g

Journal
ACS Nano, 15(4)

ISSN
1936-0851

Authors
Jacobs, Ian E
Bedolla-Valdez, Zaira I
Rotondo, Brandon T
et al.

Publication Date
2021-04-27

DOI
10.1021/acsnano.1c00070

Peer reviewed

eScholarship.org Powered by the California Digital Library
University of California

ACS NANO
www.acsnano.org

Super-Resolution Photothermal Patterning in Conductive Polymers Enabled by Thermally Activated Solubility

Ian E. Jacobs,* Zaira I. Bedolla-Valdez, Brandon T. Rotondo, David J. Bilsky, Ryan Lewis, Alejandra N. Ayala Oviedo, Goktug Gonel, John Armitage, Jun Li, and Adam J. Moulé*

Cite This: https://doi.org/10.1021/acsnano.1c00070 Read Online

ACCESS | Metrics & More | Article Recommendations | Supporting Information

ABSTRACT: **Doping-induced solubility control (DISC) patterning is a recently developed technique that uses the change in polymer solubility upon doping, along with an optical dedoping process, to achieve high-resolution optical patterning. DISC patterning can produce features smaller than predicted by the diffraction limit; however, no mechanism has been proposed to explain such high resolution. Here, we use diffraction to spatially modulate the light intensity and determine the dissolution rate, revealing a superlinear dependence on light intensity. This rate law is independent of wavelength, indicating that patterning resolution is not dominated by an optical dedoping reaction, as was previously proposed. Instead we show here that the optical patterning mechanism is primarily controlled by the thermal profile generated by the laser. To quantify this effect, the thermal profile and dissolution rate are modeled using a finite-element model and compared against patterned line cross sections as a function of wavelength, laser intensity, and dwell time. Our model reveals that although the laser-generated thermal profile is broadened considerably beyond the profile of the laser, the highly temperature dependent dissolution rate results in selective dissolution near the peak of the thermal profile. Therefore, the key factor in achieving super-resolution patterning is a strongly temperature dependent dissolution rate, a common feature of many polymers. In addition to suggesting several routes to improved resolution, our model also demonstrates that doping is not required for optical patterning of conjugated polymers, as was previously believed. Instead, we demonstrate that superlinear resolution optical patterning should be attainable in any conjugated polymer simply by tuning the solvent quality during patterning, thus extending the applicability of our method to a wide class of materials. We demonstrate the generality of photothermal patterning by writing sub-400 nm features into undoped PffBT4T-2OD.**

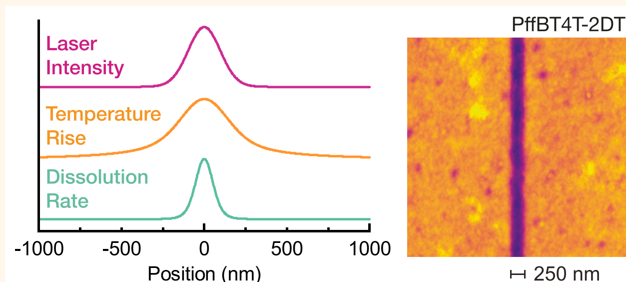

KEYWORDS: *polymers, patterning, thin films, heat transfer, photolithography*

Downloaded via UNIV OF CALIFORNIA DAVIS on April 5, 2021 at 15:53:45 (UTC).
See https://pubs.acs.org/sharingguidelines for options on how to legitimately share published articles.

Semiconducting polymers have been the focus of steadily increasing research interest for over four decades.[1] Until recently, the major research focus has been on classic optoelectronic devices such as light-emitting diodes (OLEDs),[2] thin-film transistors (OTFTs),[3−5] and photovoltaics (OPVs).[6,7] However, relatively few of these devices have reached the market due to strong competition from alternative technologies. In response, the past decade has seen the field expand to include sensors,[8,9] implantable neural interfaces,[10] spintronics,[11,12] neuromorphic computing devices,[13,14] and, most recently, electrically pumped laser diodes.[15] These devices show improved promise for industrial applications, but often involve smaller and more complex device geometries. Among the many challenges these technologies face in reaching industry scale, one of the largest needs is a universal method to produce micro- to nanoscale features for devices from semiconducting polymers cheaply, and at scale.

Unfortunately, solution processability—often touted as one of the most important features of semiconducting polymers—comes with a significant drawback. Because polymers are almost inevitably soluble in at least one step of photolithographic processes, patterning polymers on a submicron scale has been impossible without cross-linking. In more traditional

Received: January 4, 2021
Accepted: March 10, 2021

ACS Publications © XXXX American Chemical Society

devices such as OLEDs and OPVs, this is not a deal-breaker because small feature sizes are not required. However, in many emerging device applications, the inability to scale down device sizes is expected to be a major roadblock. For instance, the neuromorphic devices demonstrated by Salleo and co-workers could enable hardware-level neural computing, but are currently limited to the micron-scale due difficulty in fabricating suitably small regions of organic semiconductors.[14,16]

Even in more traditional large-area devices, the ability to pattern submicron features could allow for photonic engineering to enhance device performance. In optimized OLEDs the most significant loss mechanism is poor light outcoupling due to total internal reflection at the interface with the indium tin oxide (ITO) transparent contact. Integrating photonic structures into the active layer has been shown to significantly improve outcoupling efficiency;[17,18] however we would expect that further improvement should be possible if the ITO could be entirely replaced with a highly conductive doped polymer patterned into a photonic structure. One could imagine a similar photonic structure that improves light incoupling to the charge transfer band in organic photovoltaics.[19]

Our group recently pioneered a class of submicron patterning methods for semiconducting polymers, collectively called dopant-induced solubility control (DISC), which allow lateral and vertical patterning of conjugated polymers without chemical modification of the polymer.[20−30] DISC patterning uses charge transfer dopants to modify the solubility of the polymer: doped regions become insoluble, while undoped regions remain soluble in normal nonpolar solvents.[20] Therefore, we can pattern the polymer by generating a doping gradient and exposing the film to a good solvent for the undoped polymer.

In the highest resolution implementation of this process (shown in Figure 1a), a poly(3-hexylthiophene) (P3HT) film doped with 2,3,5,6-tetrafluoro-7,7,8,8-tetracyanoquinodimethane (F4TCNQ) is immersed in tetrahydrofuran (THF), which is a good solvent for both the neutral polymer and dopant but does not dissolve the doped film. Simultaneously, we expose the film to a 405 nm laser. The light causes a dedoping reaction to occur, resulting in dissolution of the exposed area.[20,23] Surprisingly, analysis of the spatial resolution of this process revealed that under optimized conditions the profile of the dissolved features was significantly narrower than the profile of the write laser.[21] However, in the initial publications we were unable to explain why the process achieved such high resolution.

We subsequently identified the mechanism responsible for optical dedoping, shown in Figure 1b.[23] First, an equilibrium is established between the ionized (doped) and neutral (undoped) states of the polymer and dopant molecules. Heating from the laser shifts this equilibrium toward the neutral (undoped) state due to the increased solubility of the neutral polymer/dopant at higher temperatures. As shown in Figure 1c, neutral F4TCNQ absorbs strongly at 405 nm. The resulting excited state, F4TCNQ*, quickly reacts with THF to form a nondoping product (shown bottom left in Figure 1b). This leaves the polymer in its neutral state, where it is free to dissolve into the solvent.

In standard photolithographic processes, diffraction limits the minimum periodicity of features, but not the width of the features themselves. For example, exposure just beyond the threshold allows opening of holes in the resist smaller than the

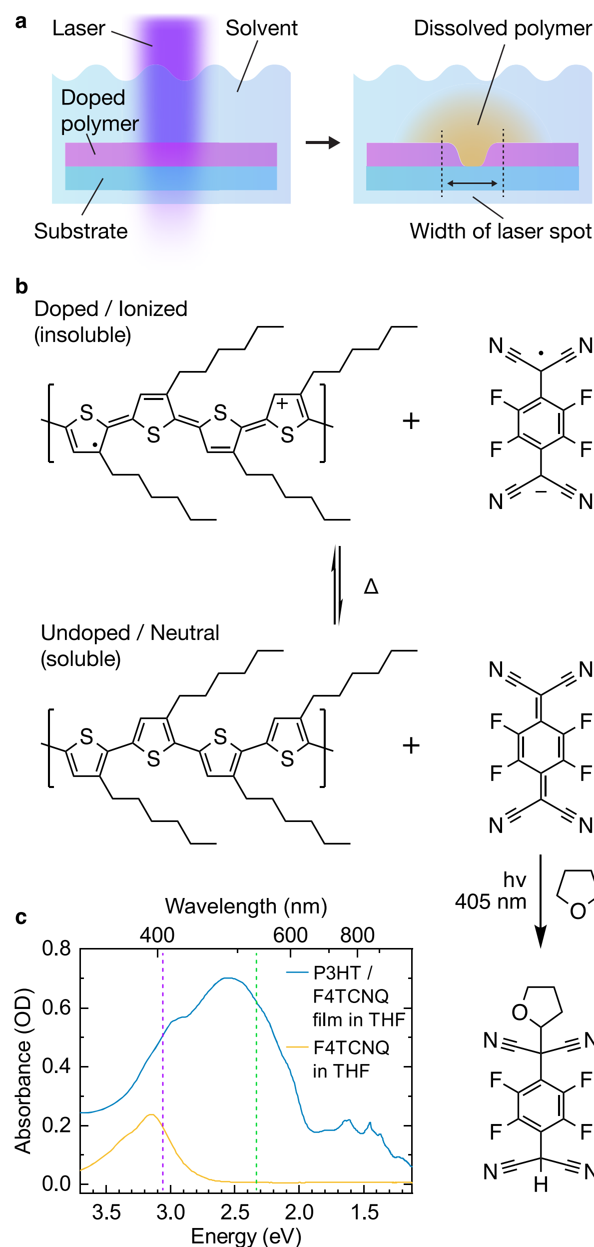

Figure 1. Overview of DISC optical patterning. (a) Schematic of the process: a focused laser illuminates a doped polymer film immersed in solvent. The exposed areas dedope and dissolve into the solvent, leaving a trench, which in some cases is narrower than the spot size of the incident laser beam. (b) Optical dedoping mechanism: an equilibrium exists between ionized polymer (P3HT) and dopant (F4TCNQ). Heating from the laser shifts the equilibrium toward the neutral species. The excited state of neutral F4TCNQ reacts with the solvent (THF) to form a nondoping species. (c) UV−vis spectrum of a P3HT:F4TCNQ film in THF, and F4TCNQ dissolved in THF. F4TCNQ absorbs strongly at 405 nm (purple dashed line) but not at 532 nm (green dashed line); the film absorption is similar at both wavelengths.

excitation spot size.[31] In DISC patterning, however, there is no resist; we directly pattern the polymeric semiconductor in a single step. Therefore, we would expect diffraction to limit the width of negative features to a size equal to the size of the excitation laser spot, given by the Rayleigh criterion $d = \frac{1.22\lambda}{\mathrm{NA}}$,

https://doi.org/10.1021/acsnano.1c00070
ACS Nano XXXX, XXX, XXX−XXX

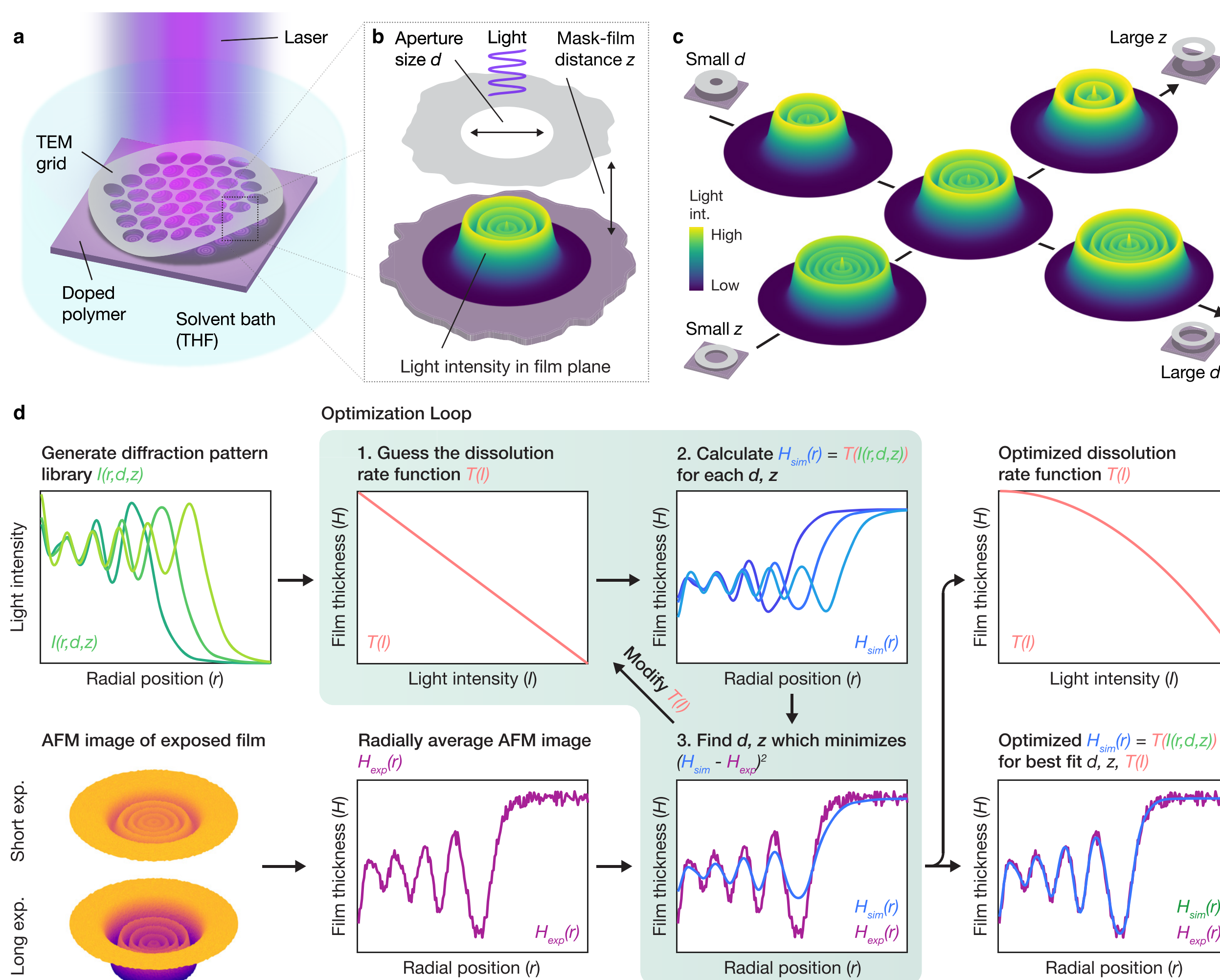

Figure 2. Method for determining the rate law. (a) Experimental setup: A P3HT:F4TCNQ film is immersed in solvent and masked by a TEM grid. Collimated 405 nm light from a diode laser is directed through the mask, producing a diffraction pattern as shown in (b). Due to manufacturing variances and micron-scale waviness in the mask, the aperture size *d* and mask−film distance *z* can vary. (c) These variations have different effects on light intensity in the film plane; therefore we can recover *d* and *z* as fit parameters. (d) Flowchart of the fitting process; discussion given in the main text.

where λ is the laser wavelength and NA is the numerical aperture of the microscope objective. To achieve feature sizes smaller than this, as previously reported, the dissolution rate must be nonlinear with respect to light intensity.[21] The mechanism shown in Figure 1b could give rise to such a nonlinearity if both the photochemical and thermal dissolution processes are linear with respect to light intensity, I, and have similar rate constants, k, giving rise to an overall rate law kI^2. We test this hypothesis by measuring the dissolution rate with respect to light intensity for 405 nm *vs* 532 nm light. As shown in Figure 1c, patterning with a 532 nm laser (green dashed line) should induce a similar degree of film heating, since the film absorptivities at 532 and 405 nm are similar. However, because F4TCNQ does not absorb at 532 nm, no photochemical reaction can occur. Su *et al.* performed a similar study, which concluded that the photochemical reaction dramatically increased the dissolution rate at moderate light intensities (<10 kW/cm^2).[30] However, they only explored the exposure required to fully dissolve the polymer and did not systematically study the resolution achievable at each wavelength or attempt to determine the dissolution rate law or underlying mechanism.

In this work, we extract the light intensity and excitation wavelength dependent dissolution rate laws in two intensity regimes: ∼1 W/cm^2 and ∼100 kW/cm^2. Using low-intensity illumination through a shadow mask, we find evidence for a nonlinear rate law for both 405 and 532 nm excitation, but with different rate constants. This suggests that the photochemical reaction of F4TCNQ increases the dissolution rate constant but does not control the overall form of the rate law. Using a high-intensity direct-write laser, the dissolution rate is similar at both wavelengths, implying that thermal dedoping and dissolution dominates the process. Thermal simulations in the high-intensity regime, supported by temperature-dependent spectroscopy, confirm that thermal dedoping dominates and enables us to give a quantitative description of dissolution in our system. We find that the primary factor that enables patterning of super-resolution feature sizes is a strongly nonlinear increase in dissolution rate with increased temperature. Additionally, our simulations indicate that our system is far from optimized, suggesting that higher resolution is possible. This quantitative model in principle allows for arbitrary modulation of polymer thickness on a submicron length scale. Such fine control of film topography is not

https://doi.org/10.1021/acsnano.1c00070
ACS Nano XXXX, XXX, XXX−XXX

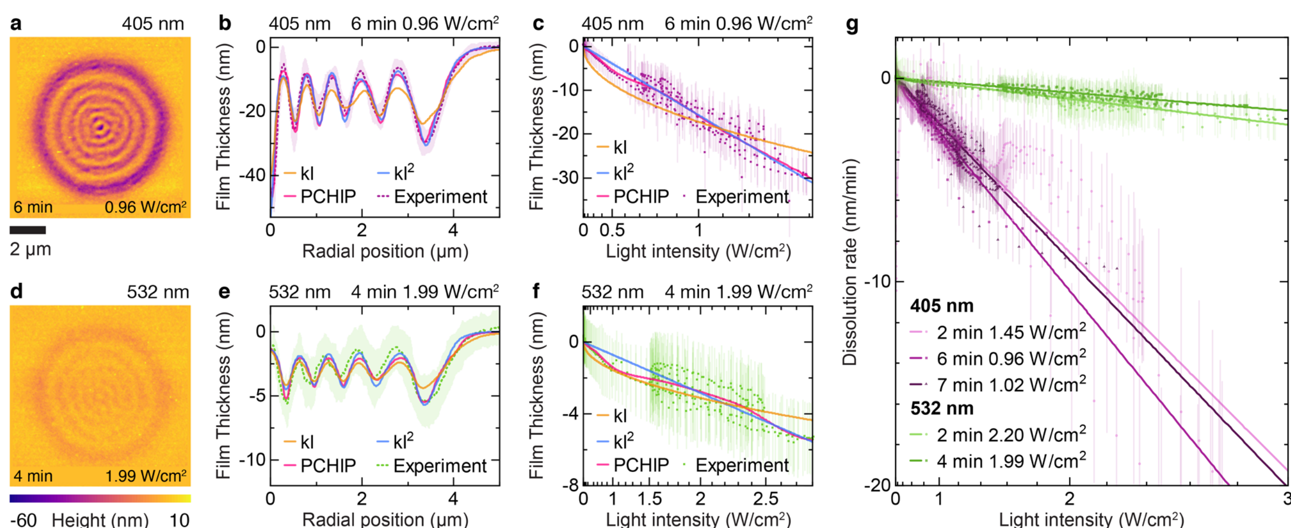

Figure 3. Determination of the rate law. (a) AFM image of a P3HT:F4TCNQ film patterned by near-field diffraction (405 nm, 0.96 W/cm², 6 min exposure). (b) Radially averaged film thickness and best fits using PCHIP (magenta), first-order (orange), and second-order (blue) transfer functions. Shaded regions represent the two standard deviation distribution of heights at each radius. (c) Scatter plot of experimental film thickness *vs* light intensity from the PCHIP fit, along with PCHIP, first-order, and second-order transfer functions. Note the quadratic scale on the *x*-axis. (d−f) Same as (a)−(c) for a P3HT:F4TCNQ pattern using green light (532 nm, 1.99 W/cm², 4 min exposure). (g) Extracted dissolution rates for 405 and 532 nm assuming a second-order rate law.

straightforward, even with normal photolithographic techniques, and could enable simpler fabrication of optical Fourier surfaces, as recently described by Lassaline *et al.*[32] These emerging materials have widespread uses in emerging photonics applications.

Furthermore, our findings demonstrate that doping is not required to achieve high-resolution optical patterning of conjugated polymers. Instead neutral polymer films can be optically patterned with similar resolution by laser heating in the presence of a marginal solvent. We illustrate this concept by demonstrating high-resolution dopant-free optical patterning of PffBT4T-2OD, a high mobility polymer with applications in photovoltaics and thin film transistors. Since strong $\pi-\pi^*$ absorption bands are a universal feature of conjugated polymers, local laser heating should always be possible. Likewise, it is always possible to tune solvent blends to control polymer solubility. We therefore expect the mechanism described here to be generally applicable to all conjugated polymers and to enable nanoscale patterning for a variety of device applications.

RESULTS AND DISCUSSION

Determining the Dissolution Rate Law at Low Light Intensity. Our first goal is to determine the relationship between light intensity and dissolution rate:

$$\frac{dH(x, y)}{dt} = T(I(x, y)) \tag{1}$$

where $H(x, y)$ is the film thickness and $T(I)$ is the dissolution rate law, which depends on the light intensity. To determine the dissolution rate law, we developed a "one-shot" measurement technique which allows us to extract the functional form of $T(I)$ from a single AFM image. In this technique, we use diffraction to spatially modulate the light intensity in the film plane, producing a corresponding spatial variation in film thickness. We then use a fitting routine to find $T(I)$, which best relates the theoretically calculated diffraction pattern to the experimentally measured image. Figure 2a shows the experimental geometry. A P3HT:F4TCNQ film is immersed in THF and masked by a TEM grid. Collimated light from a diode laser is directed through the TEM grid, producing a diffraction pattern in the plane of the film (Figure 2b). Assuming the collimated laser is sufficiently far away to be considered an incident plane wave and the film and aperture planes are parallel, we can we calculate the light intensity incident in the film plane from the Fresnel−Kirchoff diffraction formula,[33]

$$E(x, y, z) = \frac{z}{i\lambda} \iint E(x', y') \frac{e^{\frac{2\pi}{\lambda} ir}}{r^2} dx' \, dy' \tag{2}$$

where λ is the wavelength, x and y are coordinates in the film plane, x' and y' are coordinates in the aperture plane, z is the distance between the aperture plane and the film plane, $r = \sqrt{(x - x')^2 + (y - y')^2 + z^2}$ is the distance between two points in the aperture and image planes, and $E(x', y')$ is the electric field at point (x', y') in the plane of the aperture. The intensity in the film plane is then given by $I(x, y, z) = E(x, y, z)^2$. Although the Fresnel−Kirchoff integral is not rigorously accurate at very short z distances, it nonetheless shows excellent agreement with experiment when $\frac{2\pi}{\lambda}\frac{d}{2} \gg 1$, as is the case here.[34] Assuming z is small relative to the aperture lattice spacing of the TEM grid mask, the integral can be evaluated over a single aperture. This assumption is easy to confirm experimentally, since if z is greater than the lattice spacing, we observe significantly more complex interference patterns with 6-fold symmetry (see Supporting Information Figure S2).

For a circular aperture, eq 2 can be evaluated from four free parameters: wavelength (λ), incident light intensity (I_0), aperture diameter (d), and mask−film distance (z). The first two of these are easily measured; however due to manufacturing variance, the TEM grids used as the mask are not perfectly flat, and there is some variation in the diameter of the apertures (see Supporting Information Section 1.1).

Therefore, we cannot directly calculate the light intensity corresponding to a given AFM image. However, the solutions of eq 2 for d and z form an independent basis, as illustrated in Figure 2c. Qualitatively, varying d changes both the diameter of the diffraction pattern and the number of zones in the diffraction pattern, while varying z changes only the number of zones. Therefore, we can use a fitting routine to simultaneously solve for d, z, and $T(I)$.

Figure 2d shows the fitting process; further details and information on AFM processing are given in Supporting Information Section 1.3. First, we radially average the AFM image to produce a 1-D function $H_{exp}(r)$. Separately, we generate a library of 1-D diffraction patterns $I(r, d, z)$ for a range of d and z values. To fit these two data sets, we guess a rate law, $T(I)$, calculate the expected film thickness for each diffraction pattern $H_{sim}(r) = T(I(r, d, z))$, and determine the (d, z) pair that minimizes the sum of squares error (SSE) between $H_{sim}(r)$ and $H_{exp}(r)$. This process is then repeated, modifying $T(I)$ between each iteration, to find d, z, and $T(I)$, which together best fit the AFM data $H_{exp}(r)$.

Results for two of these fits are shown in Figure 3; for additional data sets see Supporting Information Section 2. Figure 3a shows a processed AFM image of a film patterned using a 405 nm laser (0.96 W/cm^2) exposed for 6 min. The radially averaged data, $H_{exp}(r)$, are shown in purple in Figure 3b. In the initial fitting, our goal was to determine the functional form of $T(I)$ without introducing significant bias. To this end, we initially defined $T(I)$ as a piecewise cubic hermite interpolating polynomial (PCHIP) spline function, which can provide a reasonable approximation of most smooth functions without introducing a functional bias. The best fit using a PCHIP function is shown in Figure 3b in magenta and represents the data well. For comparison, we also fit the data using first-order (orange) and second-order (blue) rate laws based on the incident light intensity, $T(I) = kI$ and $T(I) = kI^2$. Note that both rate laws have only a single degree of freedom: the rate constant k. The second-order fit clearly fits the data better than the first-order law, particularly at the peaks and valleys of low and high light intensity.

To better visualize how well the candidate rate laws $T(I)$ match the data, we replot the experimental data $H_{exp}(r)$, shown Figure 3b, in terms of the best fit light intensity. To do this, we need to transform $H_{exp}(r)$ into $H_{exp}(I)$, which is done by pairing the experimental height data with the best fit light intensity at each position r, *i.e.*, $H_{exp}(I) = (I(r), H_{exp}(r))$. Therefore, when each fit in Figure 3b is replotted in terms of intensity, the experimental data points are shifted horizontally according to the light intensity obtained in each fit. A good fit will result in a tight grouping of the transformed experimental data $H_{exp}(I)$ around the rate law function, while a poor fit will show more scatter. The fit quality can be quantified by the SSE, $\sum_r (H_{sim}(r) - H_{exp}(r))^2$.

Figure 3c shows the data in Figure 3b replotted as a function of the light intensity obtained from the PCHIP fit. As discussed above, it is important to note that the data in Figure 3c are simply the data in Figure 3b plotted in a different way; no additional fitting is performed in this step. Using a quadratic intensity axis, both the experimental data and the PCHIP function appear quite linear and overlap with the second-order rate law; this strongly suggests that the rate law is second-order with respect to intensity. The sum of squares error for each fit reflects these observations; while the second-order rate law SSE is slightly larger than the PCHIP fit, the first -order rate law SSE is more than 3 times larger (see Supporting Information Table S2). Results for other data sets (Supporting Information Section 2) show similar results. The second-order rate law observed here is consistent with our previous observation of line widths smaller than expected from a linear rate law.[21]

Figure 3d−f show the same analysis for a film patterned using a 532 nm laser (1.99 W/cm^2, 4 min exposure). Somewhat surprisingly, the initial PCHIP fit again shows good agreement with a second-order rate law. While a first-order intensity dependence does fit well to the low-intensity region of Figure 3f, it shows poor agreement in the high and low light intensity regions (peaks and valleys) in Figure 3e. The fit SSEs again reflect a better fit for a quadratic rate law: while the quadratic rate law (SSE = 94) is only slightly higher than the PCHIP fit (SSE = 84), the linear rate law is significantly higher (SSE = 128). Fit SSEs for all data sets are collected in Supporting Information Table S2. This nonlinear rate law is reproduced in a second data set (Supporting Information Figure S11). The observation of a second-order rate law at both 405 and 532 nm indicates that the process resolution does not depend on the photochemical reaction dedoping with F4TCNQ as previously postulated. From this, we can conclude that the laser patterning is controlled by heating of the film and subsequent dissolution of the dopant and polymer.

By repeating the procedure in Figure 3a−f for different exposure times and dividing the experimental height data H_{exp} by the exposure time, we can determine the rate constant k at each wavelength. These results, assuming a second-order rate law, are shown in Figure 3g. The tight clustering of the fits for each wavelength indicates that the process is linear with respect to time, as expected. However, as is visible by the large difference in slopes at each wavelength (which are proportional to k), dissolution is an order of magnitude faster under 405 nm illumination. From the combined data set in Figure 3g, under 405 nm illumination we obtain a rate constant $k_{405} = 2.22 \pm 0.04$ nm min^{-1} cm^4 W^{-2}, while at 532 nm, we obtain $k_{532} = 0.207 \pm 0.005$ nm min^{-1} cm^4 W^{-2}. Together, these results indicate that the photochemical reaction between F4TCNQ and THF under 405 nm illumination increases the dissolution rate, presumably by preventing dissolved (neutral) F4TCNQ from redoping the film. This conclusion is consistent with recent work by Su *et al.*, who found that at low to moderate light intensities (<10 kW/cm^2) dissolution at 405 nm was dominated by photodedoping.[30] However, since the form of the rate law is identical with or without the reaction present, it appears that the resolution of the process is entirely controlled by the thermal dedoping step shown in Figure 1.

A consequence of this conclusion—that resolution is controlled by thermal effects—is that eq 1 cannot give a comprehensive picture of the behavior of our system, because it is formulated in terms of light intensity rather than temperature. The nonidealities in our data set, for instance features in Figure 3g that could be interpreted as redeposition of polymer, further illustrate this point, since these factors will largely be controlled by thermal effects, which a model based on light intensity cannot describe. Therefore, our primary finding here—that each of our data sets (Figures S6−S12) is best fit by the same superlinear dissolution rate law—demonstrates that a model formulated in terms of temperature rather than light intensity is required.

https://doi.org/10.1021/acsnano.1c00070
ACS Nano XXXX, XXX, XXX−XXX

Dissolution at High Light Intensity. To verify that the achievable resolution is identical even in the absence of the photochemical reaction, and to better quantify the dissolution mechanism, we performed a series of patterning experiments using a laser scanning confocal microscope (LSCM) as previously described.[21] Figure 4a shows the experimental geometry. The film is coated onto microscope cover glass, which forms the bottom window of a home-built solvent cell. After filling with THF, the cell is loaded into an LSCM and exposed using the excitation beam at either 405 or 543 nm; low-intensity 633 nm excitation is used for focusing. In the absence any optical aberrations, the excitation laser is focused to a diffraction-limited Airy disk with intensity in the image plane described by

$$I(r) = I_0 \frac{2J_1\left(\frac{2\pi r}{\lambda}\text{NA}\right)}{\frac{2\pi r}{\lambda}\text{NA}} \quad (3)$$

where J_α is a Bessel function of the first kind, λ is the laser wavelength, NA is the numerical aperture of the objective, and I_0 is the incident laser intensity. The distance between the first positive and negative zeros of this function, $d = \frac{1.22\lambda}{\text{NA}}$, is known as the Rayleigh criterion and is one measure of the diffraction limit. If dissolution is linear with light intensity, eq 3 should describe the line shape of any negative feature that is not truncated by the substrate. For our setup NA = 1.42; therefore the diffraction limits at each wavelength are d_{405} = 348 nm for 405 nm light and d_{543} = 467 nm for 543 nm light. Because the spot size at 543 nm is larger than for 405 nm, for a fixed incident laser intensity I_0 the peak intensity at r = 0 will be lower at 543 nm (less optical intensity per area). To ensure the laser heating is similar at each wavelength, we adjust I_0 to match the peak intensity at each wavelength as closely as possible.

Figure 4b shows AFM images of P3HT:F4TCNQ films patterned in THF at 405 and 543 nm. The intensities shown in Figure 4 are the intensity at the center of the Airy disk, calculated using eq 3 from measurements of the integrated laser power. Figure 4c−f show the width of lines patterned for different exposure times at each wavelength and intensity as a function of percent line depth. For example, for a line 30 nm deep the width at 50% depth would correspond to the width 15 nm below the film surface. These plots allow us to visualize the resolution of the process independently from the feature depth. Also shown in each plot are diffraction-limited line widths assuming a rate law that is linear with intensity, kI (dashed line), and a rate law that is second-order with intensity, kI^2 (dotted line), calculated using eq 3.

We first compare the features patterned at lower power (144−174 kW/cm^2) shown in Figure 4c and e. At very short dwell times, <10 μs for 405 nm and <4 μs for 543 nm, no features are visible by AFM. However, at the shortest dwell times that do produce a visible feature, the line widths again closely match a second-order rate law for an aberration-free, focused laser spot (shown as dotted lines) as observed in the low-intensity diffraction data in Figure 3g. The similarity between the kinetics and resolution limit at 405 and 543 nm suggests that at the very high light intensities obtained in an LSCM, there is relatively little contribution from the photochemical dedoping reaction of F4TCNQ. Instead, the dissolution rate is almost completely thermally controlled, and the rate depends only on the heating from the laser.

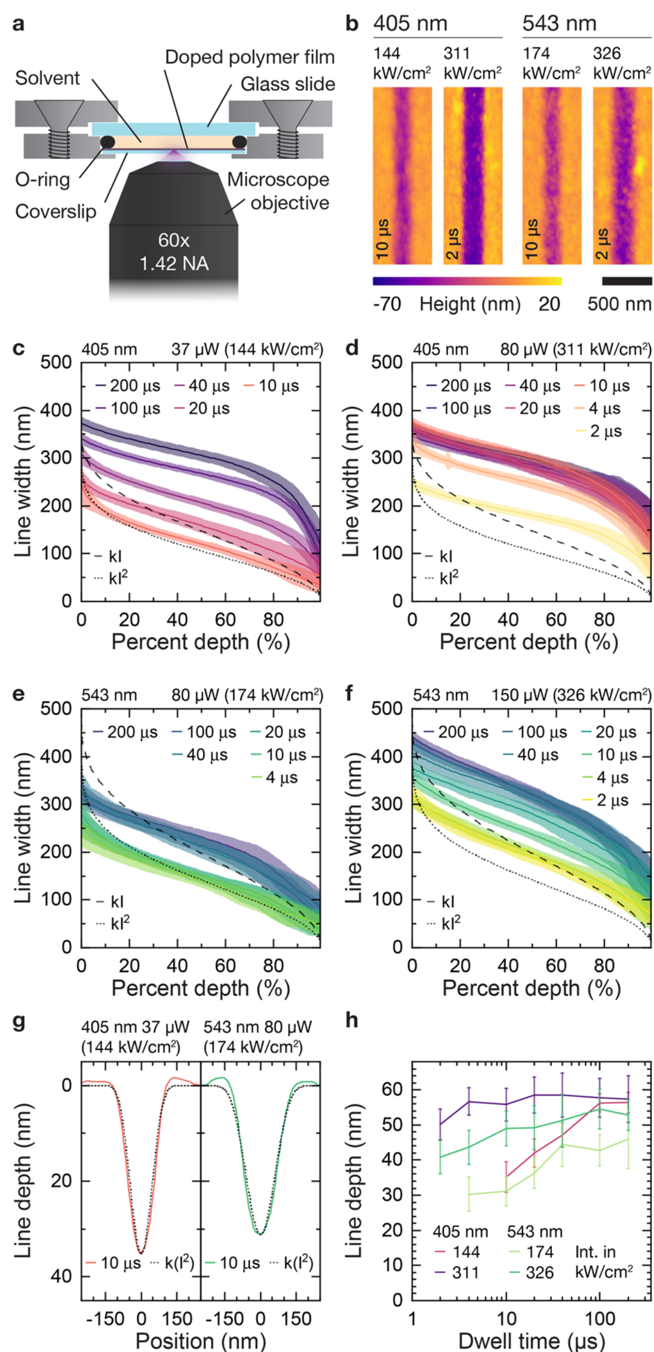

Figure 4. Effect of laser wavelength on high-intensity patterning in a LSCM. (a) Experimental setup: a P3HT:F4TCNQ film coated onto a thin microscope coverslip is sealed in a solvent cell containing THF. The film is patterned by exposure in a LSCM. (b) AFM images of lines written into a P3HT:F4TCNQ film. Laser wavelength, peak optical intensity (at the center of the laser spot), and dwell time are shown. (c−f) Extracted line widths as a function of percent of total line depth for varying dwell times. Dashed lines show the expected profile assuming a diffraction-limited laser spot without aberrations and a first-order rate law, while the dotted line shows the same for a second-order rate law. (g) 1-D projections of the narrowest features obtained at each wavelength. Dashed line shows the profile expected for a second-order rate law. (h) Line depth as a function of dwell time for each data set. Film thickness for all samples is 60 nm.

However, for longer exposure times and higher light intensities, all patterned features at both wavelengths strongly

https://doi.org/10.1021/acsnano.1c00070
ACS Nano XXXX, XXX, XXX−XXX

deviate from a second-order rate law. As shown in Supporting Information Figure S18, the line shapes in Figure 4c do not match those obtained by simply extrapolating from the second-order fits at short times to longer exposure times. In fact, to obtain these line shapes, the rate law would have to transform from superlinear to sublinear over the course of the exposure. This behavior is clearest when looking at the higher intensity laser exposure (311−326 kW/cm^2) data in Figure 4d and f, where the film thickness reaches below 20 nm. In both cases, we observe a gradual broadening near the bottom of the features, while the upper part of the features near 0% depth cluster near the diffraction-limited feature size. To obtain these line shapes, at longer exposure times the dissolution rate at the center of the laser spot must be much slower than the dissolution rate near the edges. We can also see the reduction in dissolution rate clearly in Figure 4h: feature depth is highly sublinear with light intensity. These results indicate that a rate law of the type shown in eq 1—and indeed any rate law formulated in terms of light intensity—cannot explain this regime, since direct integration of eq 1 by separation of variables yields an equation linear with respect to time.

Alternatively, if the dissolution rate is thermally controlled, we can easily explain the reduction in dissolution rate as the feature depth approaches the substrate. Very broadly, as the feature depth approaches the substrate, the film thins, absorbs less light and thus less heat, and therefore dissolves less quickly. More specifically, out-of-plane thermal transport is a sum of the thermal resistances of the polymer, interface, and substrate. However, because the polymer thermal resistance is large relative to the other two (see Supporting Information Section 4.2), the overall out-of-plane thermal transport is dependent on the polymer film thickness. As the film thins, out-of-plane transport becomes more efficient, reducing the steady-state temperature in the polymer. This reduction in temperature slows the dissolution rate, causing the self-limiting behavior observed in Figure 4.

Thermal Modeling. In order to explain the line profiles seen in Figure 4, we must reformulate the dissolution rate in terms of temperature. We do this in two steps. First, we experimentally measure the temperature-dependent polymer dissolution rate. Then, we construct a thermal model of our system, calculate the film temperature and from it the dissolution rate, and thereby accurately predict patterned line shapes.

Experimental Measurement of Thermally Activated Dissolution. To understand the effect of temperature on film solubility, we first collected temperature-dependent UV−vis−NIR spectra of a P3HT:F4TCNQ film immersed in a cuvette of THF. Figure 5a shows spectra taken through both the film and solvent, while Figure 5b shows spectra with the cuvette rotated to show the solvent only. In the film + solvent spectrum, we observe a reduction in the signals from the F4TCNQ anion (1.4 and 1.6 eV) and P3HT polaron (broad peak from 1 to 2 eV), indicating dedoping at increasing temperatures. We also observe a blue shift in the undoped polymer absorbance near 2.5 eV, indicating a reduction in the concentration of polymer crystallites as the film swells with solvent.[35]

From the solvent-only spectra, it is clearly evident that the concentration of dissolved polymer (broad peak at 2.75 eV/450 nm) in the bulk solvent dramatically increases above 40 °C. Because each temperature measurement was taken 10 min apart and the system is still far from equilibrium, we can calculate the temperature-dependent dissolution rate by measuring the change in the maximum of the dissolved polymer band between each temperature step (see Supporting Information Section 5). Polymer dissolution rates are often assumed to follow an Arrhenius-type temperature depend-

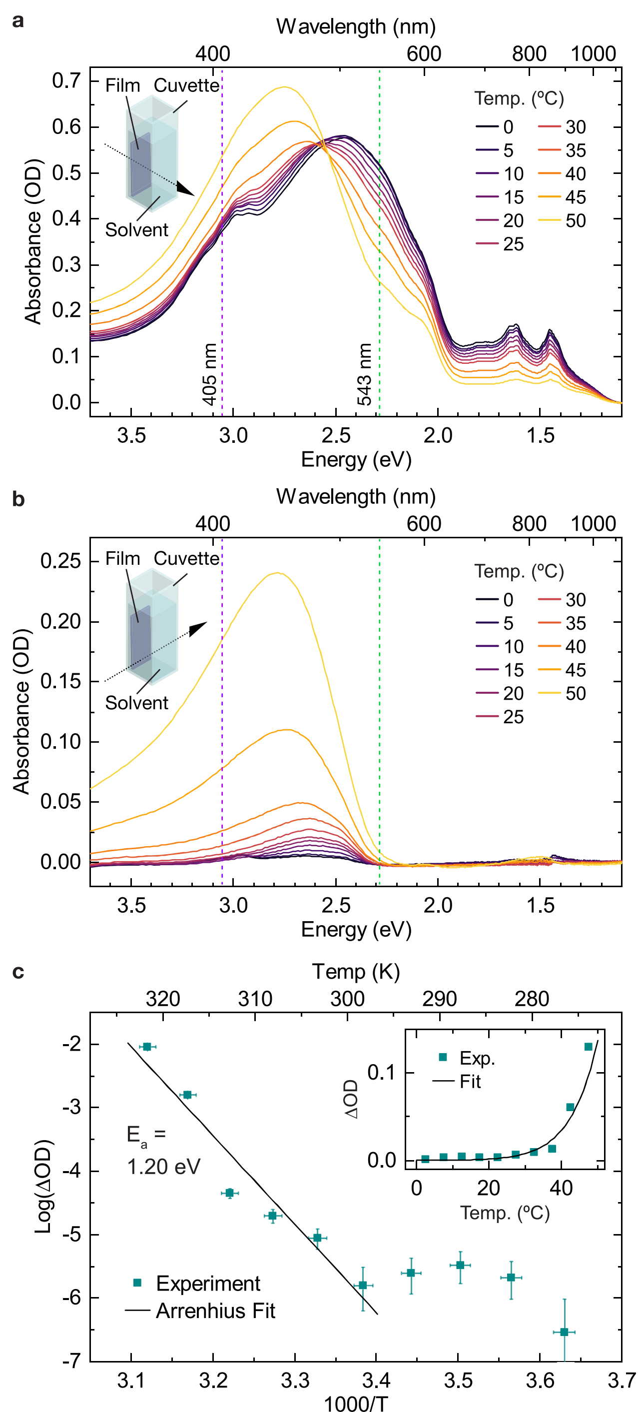

Figure 5. *T*-dependent UV−vis−NIR spectra of a P3HT:F4TCNQ film immersed in THF (see illustrations inset for measurement geometry). (a) Spectra collected through both film and solvent. (b) Spectra collected through solvent only. (c) Arrhenius plot of the change in absorbance between temperatures of the solvent-only spectrum, corresponding to the concentration of dissolved polymer. Inset shows a linear plot of change in absorbance *vs* temperature. The sample was allowed to equilibrate for 10 min between temperature steps.

https://doi.org/10.1021/acsnano.1c00070
ACS Nano XXXX, XXX, XXX−XXX

ence.[36−38] Figure 5c shows an Arrhenius plot of the change in optical density between each temperature, which is proportional to dissolution rate. Fitting the linear regime above 300 K to $\Delta OD \propto \exp(-E_a/kT)$ gives an activation energy E_a = 1.20 eV. This value is in line with those previously reported for poly(methyl methacrylate) (PMMA), which varied between 1.08 and 1.86 eV depending on processing conditions.[37] The measured activation energy is large relative to kT at room temperature (0.025 eV), which gives the dissolution rate a highly nonlinear temperature dependence, as shown in Figure 5c, inset.

Thermal Model. Having established the temperature dependence of the dissolution rate, we constructed a thermal model of our LSCM patterning experiment using finite element analysis. Our model consists of three subdomains corresponding to the solvent, film, and substrate (geometry shown in Supporting Information Figure S19). The laser is represented by a volumetric heat source within the film layer only, described by

$$q(r, z) = \frac{1}{\lambda}\exp\left(\frac{-z}{\lambda}\right)I_{Airy}(r)\, g(r, \sigma) \tag{4}$$

where λ is the attenuation length of the film at the laser wavelength, I_{Airy} is the diffraction-limited Airy disk intensity given by eq 3, and $g(r, \sigma)$ is a Gaussian function with width σ representing optical aberration. As we will discuss below, this slight broadening of the optical intensity is necessary to achieve satisfactory agreement with experimental results. Full details of the model are given in Supporting Information Section 4.

Time domain simulations between 1 ps and 1 ms reveal fast initial heating followed by a quasi-steady-state regime showing negligible thermal evolution between 2 and 200 μs (Supporting Information Figure S20). Because essentially no dissolution is observed until 4 μs in either of our low-intensity LSCM data sets, we can assume that during dissolution the temperature in the film is always at quasi-steady state.

We assume that dissolution occurs along a moving front, starting from the film−solvent interface.[38] To model dissolution, we solve for the quasi-steady-state temperature and extract the temperature at the dissolution front T_{int}. We then calculate the dissolution rate from an Arrhenius rate law:

$$\frac{dH}{dt} = A\left[\exp\left(\frac{-E_a}{kT_{int}}\right) - \exp\left(\frac{-E_a}{kT_{amb}}\right)\right] \tag{5}$$

with activation energy E_a = 1.2 eV, T_{amb} = 295 K, and A as a fit parameter. The second term of this expression sets the dissolution rate to zero at ambient temperature and can be interpreted as a redeposition rate assuming the film was in equilibrium with the solvent before the laser exposure. Note that our model does not, however, track the local concentration of polymer in the solvent phase, meaning that we are unable to describe redeposition of polymer that dissolves, then later returns to the surface. From the dissolution rate, we calculate the change in position of the dissolution front.

We have one last factor to consider: should dissolved material contribute to heating? The answer to this will depend on two factors. First, if polymer diffusion is fast on the time scale of the exposure, then obviously the polymer concentration within the patterned feature will be small and heating will be negligible. On the other hand, if diffusion is slow, we must consider how the polymer absorption spectrum changes upon dissolution. If the absorption band shifts upon dissolution, this could increase or decrease light absorption at the excitation wavelength, leading to a change in heat generation.

Comparing the absorption spectra of P3HT:F4TCNQ films and solutions in Figure 5a,b, we can clearly see that at 543 nm solvated P3HT and F4TCNQ are both essentially transparent. Therefore, regardless of diffusion rate, under 543 nm excitation the dissolved material should not contribute to heating. However, at 405 nm absorption increases somewhat after dissolution. Therefore, if polymer diffusion is slow relative to the exposure time, then at 405 nm the dissolved material should still contribute to heating.

We can estimate the diffusion length on the time scale of the exposure as $l = \sqrt{Dt}$ with t as the laser exposure time. When this value is significantly smaller than the film thickness (60 nm), the polymer has not yet had time to diffuse out of the feature and must still contribute to heating. Gu *et al.* report measurements of P3HT self-diffusion in deuterated chloroform using diffusion-ordered NMR.[39] For high molecular weight P3HT similar to that used in our study, (M_w = 51 kDa in Gu *et al.*; 65 kDa for our sample), the reported diffusion coefficient was 6.7×10^{-7} cm^2 s^{-1}. Solving for diffusion length, at 10 μs l = 26 nm, while at 200 μs l = 116 nm, indicating that diffusion is negligible for all but the longest exposure times.

Consequently, we predict that separate models will be required to fit the 405 and 543 nm data sets. The first model, which we refer to as the "absorbing solution model", includes heating by dissolved polymer within the absorption feature. The second model, which we refer to as the "transparent solution" case, simply converts the dissolved polymer to the solvent phase, as in the model by Su *et al.*[30] This should be more accurate for the 543 nm data. It is important to note, however, that the two cases we simulate here represent limiting cases of a more complex model, which explicitly accounts for solvatochromism and polymer diffusion.

We also fit our data using the model proposed by Su *et al.*;[30] however, their model is unable to quantitatively describe the dissolution features we observe. The model in Su *et al.* used a step function dissolution rate, where the rate is 0 below a threshold temperature and infinite above it. Additionally, they assumed dissolution was volumetric, so that whenever any region of the film was heated above the threshold, it instantaneously dissolved. These assumptions produce features that follow the isothermal lines in the film, with maximum width at middle depths and narrower widths near the top and bottom of the film. These predictions are inconsistent with our experimental data.

Absorbing Solution Case. To model the absorbing solution case, we treat the polymer absorption as identical before and after dissolution and neglect diffusion. While these are both approximations, at 405 nm their effects counteract each other: the absorption coefficient of the solution phase material increases, but diffusion causes the local concentration to decrease. The benefit of using these approximations is that they allow for an exceptionally simple description of polymer dissolution. Because heat generation and thermal conductivity for the entire system do not change over the course of dissolution, the quasi-steady-state temperature is also constant over the entire period. Therefore, we can completely separate polymer dissolution from the thermal model. Further details and full results are given in Supporting Information Section 4.5.

https://doi.org/10.1021/acsnano.1c00070
ACS Nano XXXX, XXX, XXX−XXX

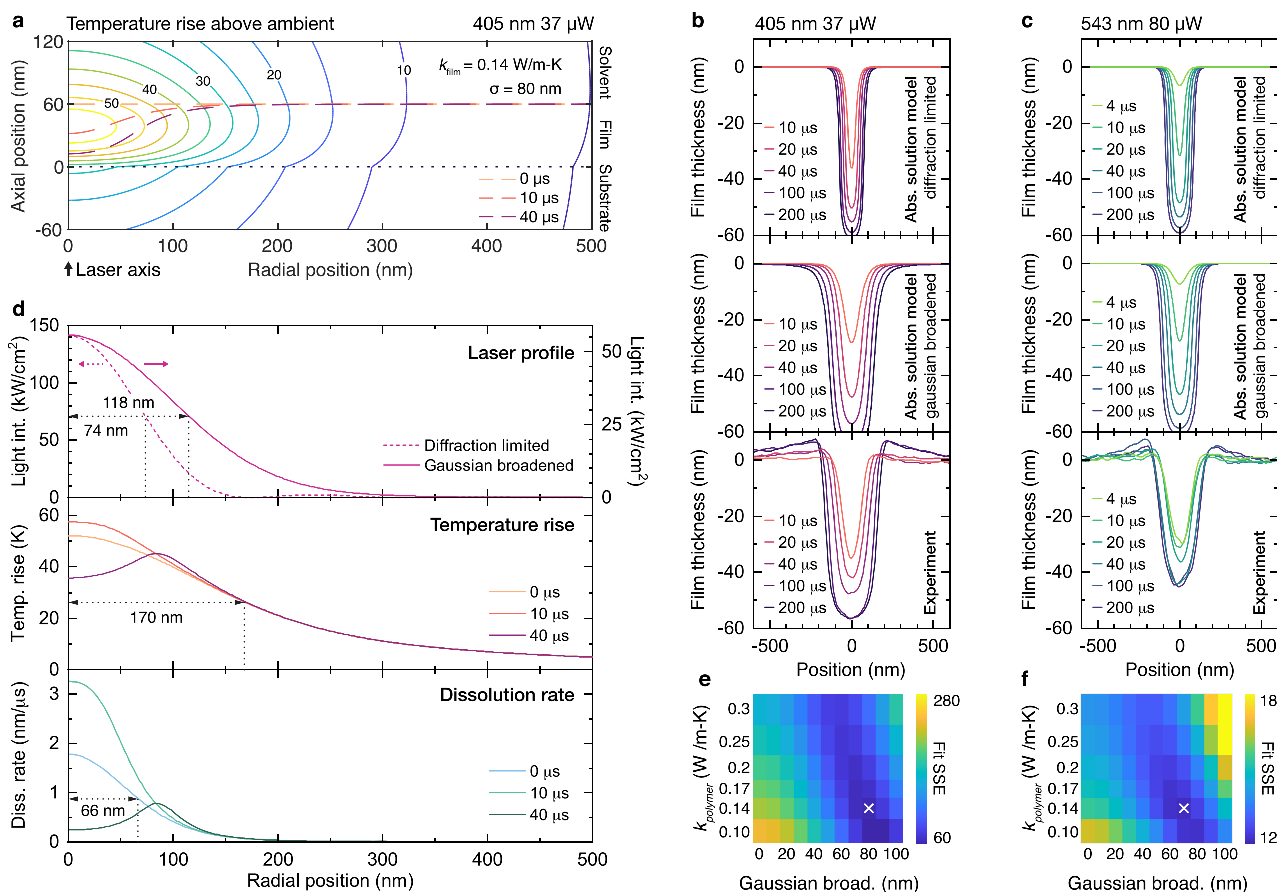

Figure 6. Thermal model of LSCM patterning, absorbing solution case. (a, b) Quasi-steady-state (2 μs) temperature map calculated using a diffraction-limited laser spot with 80 nm Gaussian broadening. Laser wavelength is 405 nm; power is 37 μW. Solid lines indicate a temperature rise above ambient in K; dashed lines show the position of the dissolution front at different times. Black dotted line shows the film−substrate interface. (b, c) Predicted and experimental film height profiles for a 405 nm, 37 μW laser (b) and a 543 nm, 80 μW laser (c). Top: Calculated profile for a diffraction-limited laser; middle: calculated profile for a Gaussian broadened laser; bottom: experimental line profile. (d) Plot of laser intensity (top), temperature at the dissolution front at various times (middle), and dissolution rate at various times (bottom). Temperatures and dissolution rates in (d) correspond to dashed lines in (a). (e, f) Maps of fit quality as a function of Gaussian broadening width and polymer thermal conductivity for a 405 nm, 37 μW laser (e) and a 543 nm, 80 μW laser (f). White "×" shows conditions corresponding to optimized Gaussian broadened fit in (b) and (c).

Figure 6a shows the quasi-steady-state temperature in the film, solvent, and substrate, assuming a film thermal conductivity of 0.14 W/(m-K) and laser Gaussian broadening of 80 nm. These parameters correspond to the best fit with experiment (Figure 6e). To calculate the dissolution dynamics, we first extract the temperature along the dissolution front, shown at various times as dashed lines in Figure 6a. These temperature values are then used to calculate the dissolution rate at each position using eq 5. Multiplying this rate by the time step gives the change in position of the dissolution front over the time step.

Figure 6b shows the best fit line shapes for the 405 nm 37 μW LSCM data set. Using a diffraction-limited laser profile (Figure 6b, top panel), our model qualitatively reproduces the experimental line shapes (bottom panel) but with feature widths that are much too narrow. Adding a Gaussian broadening to the laser source (middle panel), as noted in eq 4, widens the features and gives reasonably good agreement with the experimental data.

The residual errors in our model are largely consistent with the model's approximations. At short exposure times, our model underestimates the true feature depth, indicating that our predicted dissolution rate at short times is too small. This underestimation is expected, since the solvatochromic shift in P3HT causes an increase in light absorption upon dissolution, leading to increased heat generation. On the other hand, at longer exposure times the model overestimates the dissolution rate. Again, this is expected, since diffusion will reduce the dissolved polymer concentration at longer times, reducing heat generation. These errors demonstrate how solution absorption complicates prediction of dissolution rate and feature shape.

Figure 6e shows a heatmap of the fit SSE as a function of the film thermal conductivity and Gaussian broadening width. Our measured data are best fit by a laser source that is slightly broadened by aberration and/or misfocus. The model fit is comparatively insensitive to variation of the film thermal conductivity. The best fit thermal conductivity, 0.14 W/(m-K), is consistent with previously reported values for thin films.[40] We considered several mechanisms that could have broadened the patterned feature other than optical aberration, including variations in E_a and film thermal conductivity, and inhomogeneous (*e.g.*, vibrational) rather than optical broadening (Supporting Information Section 4.7), all of which gave lower quality fits to the measured data. The higher intensity

https://doi.org/10.1021/acsnano.1c00070
ACS Nano XXXX, XXX, XXX−XXX

405 nm data set (Figure 4d) also showed a best fit with a similar Gaussian broadening width (Supporting Information Figures S23 and S24), consistent with optical aberration rather than misfocus.

The fact that we need to broaden our model's laser source to reach good agreement with experiment is surprising, because it implies that we achieve super-resolution patterning resolution even though our optical system itself is not fully diffraction limited. Figure 6d demonstrates the mechanism for how the patterned feature can reach higher resolution than the laser itself. The top panel shows the in-plane intensity of the laser spot, assuming either diffraction-limited optics (left axis) or Gaussian-broadened optics (σ = 80 nm, right axis). Comparing the widths at half max, we see the expected ∼40 nm broadening contributed by the Gaussian blur. When the shutter is opened, the system quickly reaches quasi-steady-state condition shown in Figure 6a. The dissolution front at the start of polymer dissolution simulation is shown as the light orange dashed line in Figure 6a. The temperature along this slice is plotted in the same color in Figure 6d (middle panel), revealing an additional 55 nm of thermal broadening beyond that of the laser intensity profile. However, when we solve for the dissolution rate using this temperature profile using eq 5 we obtain the much sharper distribution shown in Figure 6d (bottom panel). The width of the dissolution rate profile is only 66 nm, even smaller the diffraction limited laser spot. The dramatic sharpening of the dissolution rate profile occurs because when $E_a \gg$ kT, eq 5 becomes extremely nonlinear with respect to temperature. This nonlinearity amplifies small differences in temperature, in effect selecting out a narrow subsection of the temperature profile for dissolution.

As dissolution proceeds, the dissolution front moves through the highest temperature region near the middle of the film (see 10 μs plots in Figure 6a and d). This ∼4 degree temperature increase causes the dissolution rate near the beam center to almost double, generating the very sharp "V"-shaped features seen in both the experimental and model line shapes at 10 μs. At longer times still (40 μs plots), the dissolution front moves into the interfacial region, where the film is efficiently cooled by the substrate. However, about 100 nm radially from the beam center the front is still within the high-temperature region (see 40 μs trace in Figure 6a), which generates an off-center peak in the temperature profile. This causes selective dissolution at the edges of the feature, which gradually transitions from a "V" into a "U" shape. Although this selective dissolution at the feature edges causes additional broadening, it also sharpens the feature edges, which is necessary for fabrication of very small positive features and deep negative features.

Returning to the fits of the 543 nm data in Figure 6c, we can immediately see that the fits are much worse than those obtained at 405 nm. Both the diffraction-limited and Gaussian-broadened models predict much steeper feature edges than observed experimentally. In addition, the feature depths vary much too strongly with exposure time. The poor fit quality here is not surprising, since the "absorbing solution model" assumes that the dissolved polymer contributes to heating, but neither P3HT or F4TCNQ absorb significantly at 543 nm when dissolved.

Transparent Solution Case. To fit the 543 nm data, we performed a series of simulations in which the dissolved material does not contribute to heating. In these simulations, we iteratively calculate the quasi-steady-state film temperature and the dissolution rate over a small time step. We then modify the simulation to treat the newly dissolved region as solvent and repeat for successive time steps. Details and full results are given in Supporting Information Section S4.6.

Figure 7a shows temperature maps of the film at quasi-steady state before any dissolution occurs, as well as at 10, 40, and 200 μs. As dissolution proceeds, the portion of the film within the laser focus quickly dissolves and causes a significant reduction in temperature because of reduced absorbance. This reduction in heating prevents the dissolution front from

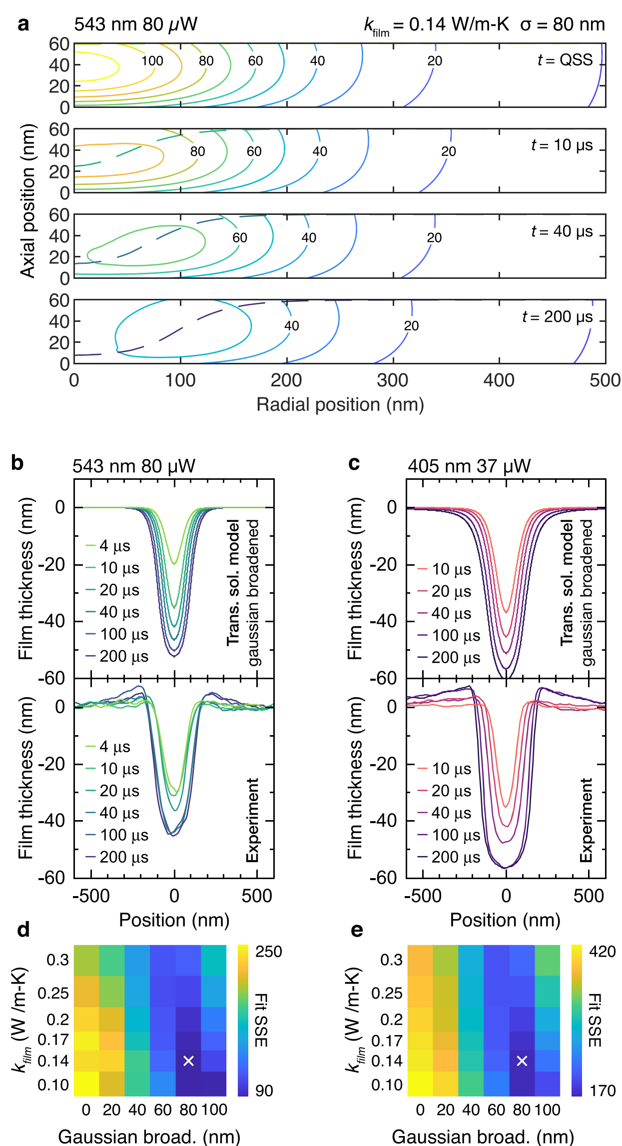

Figure 7. Thermal model of LSCM patterning, transparent solution case. (a) Temperature maps at quasi-steady state (QSS) and three different times during exposure. Solid contour lines indicate temperature rise in K; dashed lines indicate dissolution front. (b, c) Predicted and experimental film height profiles for 543 nm, 80 μW laser (d) and 405 nm, 37 μW laser exposures. Top: Calculated profile for Gaussian broadened laser; bottom: experimental line profile. (f, g) Maps of fit quality as a function of Gaussian broadening width and polymer thermal conductivity for a 543 nm, 80 μW laser (f) and a 405 nm, 37 μW laser (g). White "×" shows conditions corresponding to optimized Gaussian-broadened fit in (b) and (c).

https://doi.org/10.1021/acsnano.1c00070
ACS Nano XXXX, XXX, XXX−XXX

reaching the bottom of the film for lower laser intensity and also reduces the dissolution rate near the edges of the feature. These effects can be seen in the predicted dissolution line shapes shown in Figure 7b and c (top panels), which show a more pronounced "V" shape than those in the absorbing solution case (Figure 6b,c). Comparing the best-fit model to experiment at 543 nm in Figure 7b and d, we now see good agreement and a significant reduction in fit SSE *vs* the absorbing solution model (Figure 6c,f). The "transparent solution" model also shows very good agreement with the higher intensity 543 nm data set (Supporting Information Figures S28 and S29).

In contrast, for 405 nm excitation (Figure 7c,e), the transparent solution model gives excessively shallow feature edges, leading to much higher SSE than obtained assuming an absorbing solution. The failure of the transparent solution model in the 405 nm data set is consistent with our expectation that—for the short exposure times studied here—diffusion is sufficiently slow that absorption by the dissolved polymer cannot be neglected. However, the feature depths at longer times do show better agreement with experiment than the fits in Figure 6b, indicating that diffusion plays an increasingly important role at longer exposure times.

The self-limiting behavior seen in the transparent solution model is noteworthy because it could enable relatively simple writing of repeating surface structures, *e.g.*, for photonic structures.[32] In addition, this self-limiting behavior ensures that the remaining film is never exposed to excessively high temperatures, preventing, for example, unwanted phase transitions or chemical degradation. Lastly, comparing the transparent and absorbing solution cases, the strong self-limiting behavior seen in the transparent solution case should reduce exposure-dependent broadening, leading to narrower features. This could be achieved even at 405 nm by using longer low-intensity exposure (as would be the case for flood exposure in a mask aligner) or several short high-intensity exposures, to give the polymer time to diffuse out of the patterned features.

Both models suggest additional strategies that could be employed to further increase feature resolution. In general, these can be predicted from Figure 6d, by examining the broadening factors present. First, we could increase the resolution of the optical excitation slightly by using better quality optics, moving to shorter wavelength, or employing near-field scattering (*e.g.*, SNOM). However, these approaches are likely to be expensive and may not allow for high-throughput manufacturing.

Thermal broadening is largely controlled by the substrate and film thermal conductivities, as well as the film thickness. In device applications, film thickness and material choice will likely be constrained by other factors. However, it may be possible to use a more thermally conductive substrate, which can reduce thermal broadening by increasing the rate of out-of-plane thermal transport relative to in-plane thermal transport. Increasing the substrate thermal conductivity will also lower the temperature near the film−substrate interface. Since this heat-sinking effect is responsible for the self-limiting behavior seen in Figure 6d (and even more clearly in the transparent solution model), we expect that multiple exposures at successively higher intensity would likely be necessary when using higher thermal conductivity substrates.

Finally, increasing the dissolution activation energy will cause the dissolution rate to become more nonlinear, leading to narrower features. This will of course come at the expense of longer exposure times and higher film temperatures. A previous study on PMMA found activation energy was strongly dependent on processing conditions;[37] we would likewise expect it to vary with polymer molecular weight and solvent quality.

Self-Limiting Thermal Patterning in an Undoped Film. Having established a reasonable quantitative model that explains the writing mechanism in the LSCM, it is interesting to consider what aspects of our system enable such high resolution, and whether these results could be expanded to other material systems. As discussed previously, the most important factor is clearly a dissolution rate law that is nonlinear with respect to temperature. In addition, the film thermal conductivity should be sufficiently low relative to the substrate and interfacial thermal conductivity to prevent significant broadening of the thermal profile in the film. The polymer also must absorb at the wavelength used and convert a significant portion of that energy to heat rather than re-emitting it.

Luckily, these factors are far from unique to P3HT:F4TCNQ, or even to conductive polymers. Most polymer films have low thermal conductivity relative to inorganic substrate materials. Furthermore, solubility in most polymers is strongly temperature dependent, suggesting that dissolution activation energies are typically high. Additionally, nearly all conductive polymers have strong electronic absorption bands, and most have photoluminescence quantum yields of considerably less than 100%.

In light of the mechanistic knowledge gained here, we now understand that the role of the dopant in our previous patterning studies was primarily to increase the dissolution activation energy in a good solvent for the polymer. However, a similar effect could be achieved by using an undoped polymer and poorer quality solvent. In other words, it should be possible to pattern undoped polymers with similar resolution by simply identifying a marginal solvent. The marginal solvent must spontaneously dissolve the film at high temperatures, but prevent dissolution at room temperature.

To verify that it is indeed possible to directly pattern undoped polymer films with high resolution, we repeated the LSCM patterning experiments using films of the polymer PffBT4T-2OD, shown in Figure 8a. This material belongs to an exciting class of polymers that show excellent performance in photovoltaics and thin film transistors.[41−45] Solutions of PffBT4T-2OD show strong thermochromism due to its tendency to aggregate in room-temperature solutions.[41] To minimize dissolution at room temperature, we controlled the solvent quality by blending a good solvent with a poor solvent, which allows us to tune the temperature range over which the dissolution occurs. The patterning solvent mixture used here was a 10:1 (v/v) blend of 2-methytetrahydrofuran (mTHF) and chlorobenzene (CB). Extended soaking in this blend had no effect on film thickness or surface roughness (see Supporting Information Section 6).

Figure 8b shows lines patterned into the film using the LSCM. Rather than a single scan, as used previously, here we perform either 4 or 30 scans over the same region (see Figure 4a for experimental setup). Figure 8c shows AFM projections along the axis of the patterned line, revealing a nearly identical line profile for 4 and 30 scans. Figure 8d shows the line width *vs* percent line depth, verifying that the line shapes are effectively identical. The line width is below 400 nm at the top

https://doi.org/10.1021/acsnano.1c00070
ACS Nano XXXX, XXX, XXX−XXX

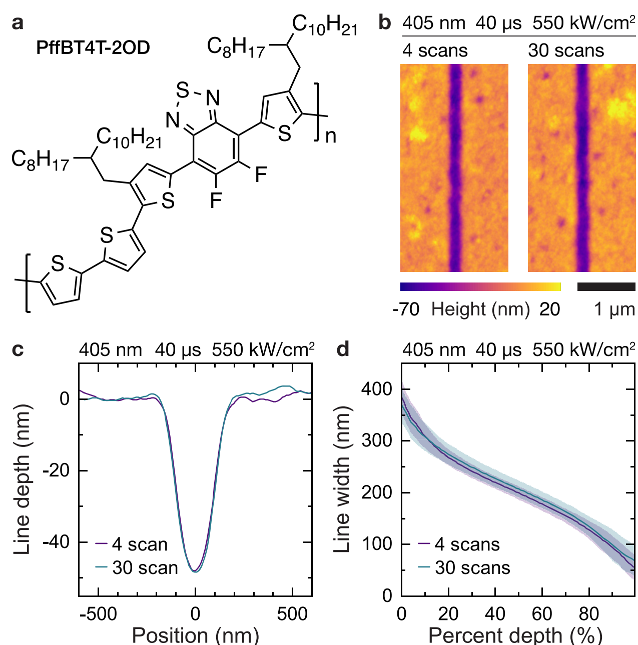

Figure 8. Dopant-free photothermal patterning. (a) Structure of PffBT4T-2OD. (b) AFM images of lines written into a PffBT4T-2OD film in mTHF:CB (10:1) using an LSCM. In the left image the laser was scanned 4 times, while in the right image the laser was scanned 30 times. (c) 1-D projection of patterned lines. (d) Extracted line width as a function of percent total line depth.

of the feature, consistent with the feature widths observed in the P3HT data patterned at 405 nm shown in Figure 4c. Together, these results are consistent with our conclusions that at high intensity optical patterning is thermally controlled and that the resolution is largely dictated by the dissolution rate law and activation energy of the polymer dissolution in the chosen solvent.

The identical profiles obtained for 4 scans *vs* 30 scans indicate that the process is entirely self-limiting and, therefore, that thermal damage from overexposure is likely to be minimal. The high resolution, simplicity, and general applicability of this purely photothermal process should extend the range of applications for semiconducting polymers.

CONCLUSIONS

We have studied the dissolution rate law for doping-induced solubility control patterning at two different exposure wavelengths and over a wide variety of exposure intensities. For small feature depths at low light intensity (~1 W/cm^2), samples patterned using both 405 and 532 nm light can be fit using a dissolution rate that is quadratic with respect to light intensity. However, the rate constant at 405 nm is approximately 1 order of magnitude higher than at 532 nm, which we attribute to a previously described photo-dedoping reaction active only at 405 nm.[23] Critically, the observation of a nonlinear rate law at both wavelengths indicates that a photochemical dedoping reaction cannot explain the sub-diffraction-limited feature sizes previously reported.[21]

At higher light intensities (~100 kW/cm^2), dissolution rates are similar at both 405 and 543 nm, indicating that localized heating dominates dissolution. Although features exposed for very short times fit well to the kI^2 rate law observed at low light intensity, this law does not fit well to features exposed for longer times. Feature depth also does not increase linearly, further indicating that the dissolution rate is not constant over time. This nonlinearity with respect to time implies that in this high-intensity regime it is not possible to describe dissolution using a rate law formulated on light intensity alone.

To fit the high intensity data, we performed thermal modeling using the finite element method. Although similar modeling was previously reported,[30] we found that several modifications were required to achieve good agreement with experiment. First, because diffusion is moderately slow on the time scale of our exposure,[39] we must account for laser heating of polymer that has dissolved, but not yet diffused out of the patterned feature. Second, we account for solvatochromism, which causes the dissolved polymer to become transparent under green light excitation but absorb strongly in the blue-violet region. Last, and most critically, we model dissolution as an interfacial process following a simple Arrenhius rate law, consistent with temperature-dependent UV−vis spectroscopy. The large activation energy we observed by UV−vis results in a strongly temperature-dependent dissolution rate. In our thermal simulations, we found that this strongly temperature dependent dissolution rate was the critical factor to achieving high-resolution photopatterning of polymer semiconductors. This rate law allows dissolution only near the peak of the temperature distribution in the film, resulting in features that are narrower than even the excitation laser profile.

Most importantly, our results reveal that photochemical dedoping—and indeed doping itself—are not prerequisites for high-resolution photothermal patterning. Rather, the only requirements are a polymer/solvent system that displays strongly temperature dependent solubility, which allows high-intensity optical excitation to induce rapid local dissolution, as we demonstrated with PffBT4T-2OD/(mTHF:CB 10:1). Because polymer solubility is very often highly temperature dependent, we expect to be able to extend this photothermal patterning process to a wide range of semiconducting polymers, and perhaps even non-semiconducting materials. The high resolution and high write speeds achievable make photothermal patterning desirable for commercial development. Because the process can use existing optical tools and does not require chemical alteration of the polymer, it should be comparatively easy and low-cost to apply in new materials systems. Together, these features make photothermal patterning an attractive fabrication method for many next-generation organic semiconductor devices, including photonic structures for photovoltaics, light-emitting diodes, and lasers, and in integrated circuits for neuromorphic devices or thin film transistors.

METHODS

Materials. Poly(3-hexylthiophene) was supplied by Plextronics with M_w = 65k. 2,3,5,6-Tetrafluoro-7,7,8,8,-tetracyanoquinodimethane (F4TCNQ, >98%) was purchased from TCI. Poly[(5,6-difluoro-2,1,3-benzothiadiazol-4,7-diyl)-*alt*-(3,3‴-di(2-octyldodecyl)-2,2′;5′,2″;5″,2‴-quaterthiophen-5,5‴-diyl)] (PffBT4T-2OD) was obtained from Lumtec. All solvents were purchased from Sigma-Aldrich.

Borosilicate glass microscope slides (Fisher Scientific) cut to required size were used as substrates, except for experiments performed in the LSCM, where 25 mm round borosilicate glass coverslips (Ted Pella, Schott D263m glass) were used. All substrates were cleaned by ultrasonication in acetone, 5% Mucasal solution, and deionized water, then dried with compressed N_2 and exposed to UV/ozone for 20 min.

Thin Film Preparation. P3HT solutions (10 mg/mL in CB) were heated at 60 °C overnight prior to use; PffBT4T-2OD was heated at 110 °C for 2 h prior to use. F4TCNQ solutions (0.1 mg/mL in acetonitrile, AN) dissolved readily and were prepared shortly before use to minimize degradation.

P3HT films were spin coated from 60 °C solutions at 1000 rpm until dry (60 s), then sequentially doped with F4TCNQ as described previously.[46] PffBT4T-2OD films were spin coated at 1000 rpm from 110 °C solution. Film thickness in both cases was 60 nm as measured by stylus profilimetry (Veeco Dektak 150).

Doping with F4TCNQ was performed on the spin coater as previously described.[46] After doping, films were rinsed with AN to remove any excess F4TCNQ that may have deposited on the film surface.

Spin coating and doping were performed in a nitrogen glovebox equipped with a molecular sieve solvent trap (<3 ppm of H_2O, O_2).

Near-Field Diffraction Patterning. Spin-coated films were removed from the glovebox and immersed in a Petri dish containing 10−20 mL of THF. A transmission electron microscopy (TEM) grid (Gilder, 2000 mesh, nickel) with a hexagonal lattice of circular holes (12.5 μm pitch with nominally 6.5 μm holes) was placed on top of the film and weighed down with a small metal washer. Illumination was provided by a collimated diode laser (∼2 mW, 405 nm) positioned ∼30 cm above the sample. The laser intensity was measured before each experiment by masking off the center of the beam with a 1.33 mm aperture and measuring the transmitted power using an optical power meter (Newport 1918 power meter and 918D-UV-OD3R photodiode).

LSCM Patterning. Samples patterned *in situ* using LSCM were prepared as described previously.[21] Briefly, P3HT films were spin-coated onto 25 mm round no. 1.5 coverslips (Schott D263m) and doped with F4TCNQ. Films were then sealed with THF in a homemade microscopy cell before removal from the glovebox. Patterning was performed on an Olympus FV1000 inverted microscope using 405 nm diode and 543 HeNe laser sources. A high numerical aperture (NA) objective (Olympus PLAPON 60XO, 1.42 NA) was used to maximize the laser intensity and resolution. Intensity was measured using a Newport 1918 power meter and 918D-UV-OD3R photodiode using defocused light from a longer working length objective (Olympus UPlanFL N 10×) and corrected for the different transmission losses between the two objectives. The 405 nm/37 μW data set was included in a previous publication.[21]

AFM Imaging. Atomic force microscopy (AFM) imaging was performed in tapping mode. Two microscopes were used. The diffraction pattern images used for rate law fitting were collected using an Asylum Research MFP3D AFM. Images of lines patterned using the LSCM were collected using a Digital Instruments Multimode AFM. BudgetSensor TAP-300G probes (300 kHz resonant frequency) were used in both cases.

UV−Vis Spectroscopy. P3HT:F4TCNQ films were prepared as described above on 9.5 by 25 mm substrates and placed inside a 10 mm quartz fluorescence cuvette filled with cold THF, then capped and sealed with Teflon tape. Temperature-dependent UV−vis spectra were collected on a PerkinElmer Lambda 750 using a home-built temperature control system. Thermal control was provided by an SP Scientific AirJet XE using a thermocouple in contact with the underside of the cuvette. Spectra were collected every 5 degrees on a heating scan, allowing the sample to equilibrate for 5 min between temperature points. At each temperature point, two spectra were taken: one with the film sample in the beam path and one with the cuvette rotated 90 deg to allow measurement of the solvent only. Total measurement time between data points was 10 min.

ASSOCIATED CONTENT

Supporting Information

The Supporting Information is available free of charge at https://pubs.acs.org/doi/10.1021/acsnano.1c00070.

Details and full results of diffraction pattern fitting routine, LSCM sample data processing, complete details of the thermal model, additional information regarding temperature-dependent UV−vis, and AFM images of solvent-exposed PffBT4T-2OD films, including Figures S1−S34 and Tables S1−S5 (PDF)

AUTHOR INFORMATION

Corresponding Authors

Ian E. Jacobs − *Department of Materials Science and Engineering, University of California Davis, Davis, California 95616, United States; Optoelectronics Group, Cavendish Laboratory, University of Cambridge, Cambridge CB3 0HE, U.K.;* orcid.org/0000-0002-1535-4608; Email: ij255@cam.ac.uk

Adam J. Moulé − *Department of Chemical Engineering, University of California Davis, Davis, California 95616, United States;* orcid.org/0000-0003-1354-3517; Email: amoule@ucdavis.edu

Authors

Zaira I. Bedolla-Valdez − *Department of Chemical Engineering, University of California Davis, Davis, California 95616, United States*

Brandon T. Rotondo − *Department of Chemical Engineering, University of California Davis, Davis, California 95616, United States*

David J. Bilsky − *Department of Chemical Engineering, University of California Davis, Davis, California 95616, United States*

Ryan Lewis − *Department of Chemical Engineering, University of California Davis, Davis, California 95616, United States*

Alejandra N. Ayala Oviedo − *Department of Chemical Engineering, University of California Davis, Davis, California 95616, United States*

Goktug Gonel − *Department of Chemical Engineering, University of California Davis, Davis, California 95616, United States*

John Armitage − *Optoelectronics Group, Cavendish Laboratory, University of Cambridge, Cambridge CB3 0HE, U.K.*

Jun Li − *Department of Chemical Engineering, University of California Davis, Davis, California 95616, United States;* orcid.org/0000-0001-7850-3722

Complete contact information is available at: https://pubs.acs.org/10.1021/acsnano.1c00070

Notes

The authors declare no competing financial interest.

ACKNOWLEDGMENTS

This project was initiated with funding from the U.S. Department of Energy, Office of Basic Energy Sciences, Division of Materials Sciences and Engineering, under Award No. DE-SC0010419. All data taken on doped P3HT films at low light intensity were collected with DOE funding. Later experiments involving high light intensity irradiation and PffBT4T-2OD were carried out with support from the National Science Foundation Award No. 1636385. Z.I.B.V. thanks SENER-CONACyT project no. 291145 for postdoctoral support. I.E.J. acknowledges funding by a Royal Society Newton International Fellowship during part of the manuscript preparation. I.E.J. also thanks M. Millea and A. Bradshaw for helpful discussions. The authors would also like to acknowl-

edge the Keck Spectral Imaging Facility, NEAT-ORU UC Davis, for use of the LSCM and AFM.

REFERENCES

(1) Heeger, A. J. Semiconducting Polymers: The Third Generation. *Chem. Soc. Rev.* **2010**, *39*, 2354−2371.
(2) Burroughes, J. H.; Bradley, D. D. C.; Brown, A. R.; Marks, R. N.; Mackay, K.; Friend, R. H.; Burns, P. L.; Holmes, A. B. Light-Emitting Diodes Based on Conjugated Polymers. *Nature* **1990**, *347*, 539−541.
(3) Bao, Z.; Dodabalapur, A.; Lovinger, A. J. Soluble and Processable Regioregular Poly (3-Hexylthiophene) for Thin Film Field-Effect Transistor Applications with High Mobility. *Appl. Phys. Lett.* **1996**, *69*, 4108−4110.
(4) Sirringhaus, H.; Brown, P. J.; Friend, R. H.; Nielsen, M. M.; Bechgaard, K.; Langeveld-Voss, B. M. W.; Spiering, A. J. H.; Janssen, R. A. J.; Meijer, E. W.; Herwig, P.; de Leeuw, D. M. Two-Dimensional Charge Transport in Self-Organized, High-Mobility Conjugated Polymers. *Nature* **1999**, *401*, 685−688.
(5) Sirringhaus, H. Device Physics of Solution-Processed Organic Field-Effect Transistors. *Adv. Mater.* **2005**, *17*, 2411−2425.
(6) Yu, G.; Gao, J.; Hummelen, J. C.; Wudl, F.; Heeger, A. J. Polymer Photovoltaic Cells: Enhanced Efficiencies *via* a Network of Internal Donor-Acceptor Heterojunctions. *Science* **1995**, *270*, 1789−1791.
(7) Günes, S.; Neugebauer, H.; Sariciftci, N. S. Conjugated Polymer-Based Organic Solar Cells. *Chem. Rev.* **2007**, *107*, 1324−1338.
(8) Mabeck, J. T.; Malliaras, G. G. Chemical and Biological Sensors Based on Organic Thin-Film Transistors. *Anal. Bioanal. Chem.* **2005**, *384*, 343−353.
(9) Rivnay, J.; Inal, S.; Salleo, A.; Owens, R. M.; Berggren, M.; Malliaras, G. G. Organic Electrochemical Transistors. *Nat. Rev. Mater.* **2018**, *3*, 17086.
(10) Khodagholy, D.; Doublet, T.; Quilichini, P.; Gurfinkel, M.; Leleux, P.; Ghestem, A.; Ismailova, E.; Hervé, T.; Sanaur, S.; Bernard, C.; Malliaras, G. G. *In Vivo* Recordings of Brain Activity Using Organic Transistors. *Nat. Commun.* **2013**, *4*, 1575.
(11) Dediu, V. A.; Hueso, L. E.; Bergenti, I.; Taliani, C. Spin Routes in Organic Semiconductors. *Nat. Mater.* **2009**, *8*, 707.
(12) Wang, S.-J.; Venkateshvaran, D.; Mahani, M. R.; Chopra, U.; McNellis, E. R.; Di Pietro, R.; Schott, S.; Wittmann, A.; Schweicher, G.; Cubukcu, M.; Kang, K.; Carey, R.; Wagner, T. J.; Siebrecht, J. N. M.; Wong, D. P. G. H.; Jacobs, I. E.; Aboljadayel, R. O.; Ionescu, A.; Egorov, S. A.; Mueller, S.; et al. Long Spin Diffusion Lengths in Doped Conjugated Polymers Due to Enhanced Exchange Coupling. *Nat. Electron.* **2019**, *2*, 98−107.
(13) van de Burgt, Y.; Lubberman, E.; Fuller, E. J.; Keene, S. T.; Faria, G. C.; Agarwal, S.; Marinella, M. J.; Alec Talin, A.; Salleo, A. A Non-Volatile Organic Electrochemical Device as a Low-Voltage Artificial Synapse for Neuromorphic Computing. *Nat. Mater.* **2017**, *16*, 414.
(14) van de Burgt, Y.; Melianas, A.; Keene, S. T.; Malliaras, G.; Salleo, A. Organic Electronics for Neuromorphic Computing. *Nat. Electron.* **2018**, *1*, 386−397.
(15) Sandanayaka, A. S. D.; Matsushima, T.; Bencheikh, F.; Terakawa, S.; Potscavage, W. J.; Qin, C.; Fujihara, T.; Goushi, K.; Ribierre, J.-C.; Adachi, C. Indication of Current-Injection Lasing from an Organic Semiconductor. *Appl. Phys. Express* **2019**, *12*, 061010.
(16) Fuller, E. J.; Keene, S. T.; Melianas, A.; Wang, Z.; Agarwal, S.; Li, Y.; Tuchman, Y.; James, C. D.; Marinella, M. J.; Yang, J. J.; Salleo, A.; Talin, A. A. Parallel Programming of an Ionic Floating-Gate Memory Array for Scalable Neuromorphic Computing. *Science* **2019**, *364*, 570.
(17) Sun, Y.; Forrest, S. R. Enhanced Light Out-Coupling of Organic Light-Emitting Devices Using Embedded Low-Index Grids. *Nat. Photonics* **2008**, *2*, 483.
(18) Meerholz, K.; Muller, D. C. Outsmarting Waveguide Losses in Thin-Film Light-Emitting Diodes. *Adv. Funct. Mater.* **2001**, *11*, 251−253.
(19) Siegmund, B.; Mischok, A.; Benduhn, J.; Zeika, O.; Ullbrich, S.; Nehm, F.; Böhm, M.; Spoltore, D.; Fröb, H.; Körner, C.; Leo, K.; Vandewal, K. Organic Narrowband Near-Infrared Photodetectors Based on Intermolecular Charge-Transfer Absorption. *Nat. Commun.* **2017**, *8*, 15421.
(20) Jacobs, I. E.; Li, J.; Burg, S. L.; Bilsky, D. J.; Rotondo, B. T.; Augustine, M. P.; Stroeve, P.; Moulé, A. J. Reversible Optical Control of Conjugated Polymer Solubility with Sub-Micrometer Resolution. *ACS Nano* **2015**, *9*, 1905−1912.
(21) Jacobs, I. E.; Aasen, E. W.; Nowak, D.; Li, J.; Morrison, W.; Roehling, J. D.; Augustine, M. P.; Moulé, A. J. Direct-Write Optical Patterning of P3HT Films beyond the Diffraction Limit. *Adv. Mater.* **2017**, *29*, 1603221.
(22) Jacobs, I. E.; Moulé, A. J. Controlling Molecular Doping in Organic Semiconductors. *Adv. Mater.* **2017**, *29*, 1703063.
(23) Fuzell, J.; Jacobs, I. E.; Ackling, S.; Harrelson, T. F.; Huang, D. M.; Larsen, D.; Moulé, A. J. Optical Dedoping Mechanism for P3HT:F4TCNQ Mixtures. *J. Phys. Chem. Lett.* **2016**, *7*, 4297−4303.
(24) Jacobs, I. E.; Wang, F.; Hafezi, N.; Medina-Plaza, C.; Harrelson, T. F.; Li, J.; Augustine, M. P.; Mascal, M.; Moulé, A. J. Quantitative Dedoping of Conductive Polymers. *Chem. Mater.* **2017**, *29*, 832−841.
(25) Li, J.; Holm, D. M.; Guda, S.; Bedolla-Valdez, Z. I.; Gonel, G.; Jacobs, I. E.; Dettmann, M. A.; Saska, J.; Mascal, M.; Moulé, A. J. Effect of Processing Conditions on Additive DISC Patterning of P3HT Films. *J. Mater. Chem. C* **2019**, *7*, 302−313.
(26) Murrey, T. L.; Guo, K.; Mulvey, J. T.; Lee, O. A.; Cendra, C.; Bedolla-Valdez, Z. I.; Salleo, A.; Moulin, J.-F.; Hong, K.; Moulé, A. J. Additive Solution Deposition of Multi-Layered Semiconducting Polymer Films for Design of Sophisticated Device Architectures. *J. Mater. Chem. C* **2019**, *7*, 953−960.
(27) Park, S.; Yu, S. H.; Kim, J.; Kang, M.; Sim, K. M.; Chung, D. S. Iodine-Mediated Non-Destructive Multilayer Stacking of Polymer Semiconductors for Near-Infrared-Selective Photodiode. *Org. Electron.* **2019**, *68*, 63−69.
(28) Kang, M.; Yoon, S.; Cho, J.; Kim, J.; Chung, D. S. Reactive Dedoping of Polymer Semiconductors to Boost Self-Powered Schottky Diode Performances. *ACS Appl. Mater. Interfaces* **2019**, *11*, 8365−8373.
(29) Kim, J.; Kang, M.; Cho, J.; Yu, S. H.; Chung, D. S. Doping−Dedoping Interplay to Realize Patterned/Stacked All-Polymer Optoelectronic Devices. *ACS Appl. Mater. Interfaces* **2019**, *11*, 18580−18589.
(30) Su, Z.; Bedolla-Valdez, Z. I.; Wang, L.; Rho, Y.; Chen, S.; Gonel, G.; Taurone, E. N.; Moulé, A. J.; Grigoropoulos, C. P. High-Speed Photothermal Patterning of Doped Polymer Films. *ACS Appl. Mater. Interfaces* **2019**, *11*, 41717−41725.
(31) Fischer, J.; Wegener, M. Three-Dimensional Optical Laser Lithography beyond the Diffraction Limit. *Laser Photonics Rev.* **2013**, *7*, 22−44.
(32) Lassaline, N.; Brechbühler, R.; Vonk, S. J. W.; Ridderbeek, K.; Spieser, M.; Bisig, S.; le Feber, B.; Rabouw, F. T.; Norris, D. J. Optical Fourier Surfaces. *Nature* **2020**, *582*, 506−510.
(33) Born, M.; Wolf, E. *Principles of Optics: Electromagnetic Theory of Propagation, Interference and Diffraction of Light*; Cambridge University Press: Cambridge, 1999.
(34) Wolf, E.; Marchand, E. W. Comparison of the Kirchhoff and the Rayleigh−Sommerfeld Theories of Diffraction at an Aperture. *J. Opt. Soc. Am.* **1964**, *54*, 587−594.
(35) Clark, J.; Chang, J.-F.; Spano, F. C.; Friend, R. H.; Silva, C. Determining Exciton Bandwidth and Film Microstructure in Polythiophene Films Using Linear Absorption Spectroscopy. *Appl. Phys. Lett.* **2009**, *94*, 163306.
(36) Greeneich, J. S. Developer Characteristics of Poly-(Methyl Methacrylate) Electron Resist. *J. Electrochem. Soc.* **1975**, *122*, 970.
(37) Manjkow, J. Influence of Processing and Molecular Parameters on the Dissolution Rate of Poly-(Methyl Methacrylate) Thin Films. *J. Electrochem. Soc.* **1987**, *134*, 2003.
(38) Miller-Chou, B. A.; Koenig, J. L. A Review of Polymer Dissolution. *Prog. Polym. Sci.* **2003**, *28*, 1223−1270.

https://doi.org/10.1021/acsnano.1c00070
ACS Nano XXXX, XXX, XXX−XXX

(39) Gu, K.; Onorato, J.; Xiao, S. S.; Luscombe, C. K.; Loo, Y.-L. Determination of the Molecular Weight of Conjugated Polymers with Diffusion-Ordered NMR Spectroscopy. *Chem. Mater.* **2018**, *30*, 570−576.
(40) Rausch, S.; Rauh, D.; Deibel, C.; Vidi, S.; Ebert, H. P. Thin-Film Thermal-Conductivity Measurement on Semi-Conducting Polymer Material Using the 3ω Technique. *Int. J. Thermophys.* **2013**, *34*, 820−830.
(41) Liu, Y.; Zhao, J.; Li, Z.; Mu, C.; Ma, W.; Hu, H.; Jiang, K.; Lin, H.; Ade, H.; Yan, H. Aggregation and Morphology Control Enables Multiple Cases of High-Efficiency Polymer Solar Cells. *Nat. Commun.* **2014**, *5*, 5293.
(42) Zhao, J.; Li, Y.; Lin, H.; Liu, Y.; Jiang, K.; Mu, C.; Ma, T.; Lin Lai, J. Y.; Hu, H.; Yu, D.; Yan, H. High-Efficiency Non-Fullerene Organic Solar Cells Enabled by a Difluorobenzothiadiazole-Based Donor Polymer Combined with a Properly Matched Small Molecule Acceptor. *Energy Environ. Sci.* **2015**, *8*, 520−525.
(43) Zhao, J.; Li, Y.; Yang, G.; Jiang, K.; Lin, H.; Ade, H.; Ma, W.; Yan, H. Efficient Organic Solar Cells Processed from Hydrocarbon Solvents. *Nat. Energy* **2016**, *1*, 15027.
(44) Li, Z.; Jiang, K.; Yang, G.; Lai, J. Y. L.; Ma, T.; Zhao, J.; Ma, W.; Yan, H. Donor Polymer Design Enables Efficient Non-Fullerene Organic Solar Cells. *Nat. Commun.* **2016**, *7*, 13094.
(45) Li, M.; Mangalore, D. K.; Zhao, J.; Carpenter, J. H.; Yan, H.; Ade, H.; Yan, H.; Müllen, K.; Blom, P. W. M.; Pisula, W.; de Leeuw, D. M.; Asadi, K. Integrated Circuits Based on Conjugated Polymer Monolayer. *Nat. Commun.* **2018**, *9*, 451.
(46) Jacobs, I. E.; Aasen, E. W.; Oliveira, J. L.; Fonseca, T. N.; Roehling, J. D.; Li, J.; Zhang, G.; Augustine, M. P.; Mascal, M.; Moule, A. J. Comparison of Solution-Mixed and Sequentially Processed P3HT:F4TCNQ Films: Effect of Doping-Induced Aggregation on Film Morphology. *J. Mater. Chem. C* **2016**, *4*, 3454−3466.

https://doi.org/10.1021/acsnano.1c00070
ACS Nano XXXX, XXX, XXX−XXX